Journal of Alloys and Compounds 1010 (2025) 178088

Contents lists available at ScienceDirect

Journal of Alloys and Compounds

journal homepage: www.elsevier.com/locate/jalcom

Hardenability and microstructural evolution of a precipitation strengthened $Ni_{50}Ti_{21}Hf_{25}Al_4$ alloy

Flavia da Cruz Gallo [a], Yang Yang [a], Eitan Hershkovitz [a], Monica Kapoor [a], Hunter B. Henderson [b], Michael S. Kesler [c], Honggyu Kim [a], Michele V. Manuel [d,*]

[a] *University of Florida, Department of Materials Science and Engineering, 549 Gale Lemerand Drive, Gainesville, FL 32611-2049, USA*
[b] *Lawrence Livermore National Laboratory, 7000 East Ave, Livermore, CA 94550, USA*
[c] *Oak Ridge National Laborator, Materials Science and Technology Division, 1 Bethel Valley Rd, Oak Ridge, TN 37831, USA*
[d] *University of Pittsburgh, Department of Mechanical Engineering and Materials Science, 109 Benedum Hall, Pittsburgh, PA 15261, USA*

ARTICLE INFO

Keywords:
Shape memory alloy
Heusler phase precipitate
H-phase precipitate
Precipitation strengthening
Transmission electron microscopy

ABSTRACT

NiTi-based quaternary alloys are used in a variety of mechanical components, such as bearings, actuators, and dampers, owing to their good hardenability, wear resistance, and corrosion resistance. Additionally, one of the most notable characteristics of NiTi-based alloys is their shape memory effect and pseudoelastic properties. Connecting the macroscopic processing parameters employed in the design of new intermetallic alloys to the nanoscale structural characteristics dictating their behavior is crucial for improving their mechanical properties and expanding the spectrum of potential applications. In this work, an arc melted $Ni_{50}Ti_{21}Hf_{25}Al_4$ (at%) alloy was solution treated at 1050 °C followed by quenching and aging at 600 °C to investigate the effect of aging time on the microstructure and mechanical properties. Two types of nano-sized precipitates were observed and determined as face-centered orthorhombic H-phase (TiHf)Ni and $L2_1$ Heusler precipitates Ni_2TiAl. The morphology and orientation of the H-phase were investigated using scanning and transmission electron microscopy (SEM and TEM), elucidating the coarsening kinetics and strengthening contribution of that phase to the intermetallic mechanical behavior. Following coarsening, the presence of Heusler nanoprecipitates was detected under overaged conditions through TEM imaging and nanobeam electron diffraction patterns. A peak hardness condition of 756 HV was achieved after 70 h of aging, indicating that the co-precipitation of H-phase and Heusler precipitates through a well-designed aging treatment can lead to optimal mechanical performance, thus elevating the alloy's potential as a viable material for industrial applications.

1. Introduction

NiTi-based metallic alloys are required to exhibit superior thermomechanical behavior to fully leverage their functional properties, thereby expanding their applications across diverse areas [1–3]. Aerospace, automotive, and oil and gas industries require properties such as hardness, strength, toughness, and work output, which can be greatly improved by precipitate strengthening [4–6]. As strengthening increases the stress required for the onset of plastic deformation, it is beneficial for shape recovery in shape memory alloys (SMAs) [7]. However, introducing a non-transforming second phase within a shape memory matrix can lead to strain localization and ultimately plastic deformation, thus reducing the material's overall performance [8,9]. This can be mitigated through the introduction of highly coherent precipitates that generate less localized strain during phase transformation [10–12].

There is significant interest in investigating the effect of ternary and quaternary element additions [13–20] for improved SMA performance. For example, in the development of high-temperature SMAs, Hf and Zr additions have been explored [21–23]. However, NiTiZr alloys produce undesirable Laves phases after aging, causing embrittlement [24]. The literature shows that the addition of more than 3 % of Hf, substituting Ti in a $Ni_{49}Ti_{51}$ (all compositions will be reported in at%) alloy, increases the martensitic transformation temperature, reaching a peak transformation temperature of 622 °C in the 30 % Hf alloy [25]. Moreover, NiTiHf system can be age-hardened in the temperature range of 400 – 650 °C to precipitate the orthorhombic lenticular-shaped precipitate

---

* Corresponding author.
E-mail addresses: fdacruzgallo@ufl.edu (F. da Cruz Gallo), yangyang2@ufl.edu (Y. Yang), ehershkovitz@ufl.edu (E. Hershkovitz), monica.kapoor@ufl.edu (M. Kapoor), henderson67@llnl.gov (H.B. Henderson), keslerms@ornl.gov (M.S. Kesler), honggyukim@ufl.edu (H. Kim), mmanuel@pitt.edu (M.V. Manuel).

https://doi.org/10.1016/j.jallcom.2024.178088
Received 11 July 2024; Received in revised form 14 November 2024; Accepted 12 December 2024

known as the H-phase (or Han-phase) with the nominal composition of $(Ti_{0.6}Hf_{0.4})Ni$ [6,26]. Previous studies argue that the precipitation of the H-phase in a NiTiHf alloy enhances both strength and superelastic behaviors [27,28]. Despite the significant impact of the H-phase on the properties of NiTi-based SMAs, a comprehensive understanding of its structure remains limited.

The addition of Al in the NiTi system has been reported to result in controlled precipitation of nanoscale coherent Ni_2TiAl precipitates from a supersaturated B2 NiTi-based matrix [12,19,29]. This precipitate is known as the Heusler phase and adopts an $L2_1$ crystal structure [30,31]. The coherent precipitation of the Heusler phase has been found to significantly increase the compressive strength by an order of magnitude in a $Ni_{50.7}Ti_{40.9}Al_{8.4}$ alloy [32], demonstrating the precipitates' capability to strengthen the alloy. However, the addition of Al is also associated with lowering the martensitic transformation temperature in equiatomic NiTi alloy [33]. Additionally, the ductility of $Ni_{50.7}Ti_{40.9}Al_{8.4}$ alloys at room temperature decreases with increasing Al content [32].

Taking advantages of Al and Hf additions into the NiTi system, Jung *et al.* [29] conducted one of the initial studies on incorporating Hf into NiTiAl alloys. They found that addition of 5 at% Hf, substituting Ti, to a $Ni_{50}Ti_{45}Al_5$ alloy resulted in precipitation of uniformly distributed Heusler phase after aging at 600°C. The Heusler precipitate was found to have slow coarsening rates, which was attributed to Hf partitioning to the Heusler phase, lowering the lattice misfit between the precipitate and the matrix [29]. While Jung *et al.'s* study served as an important starting point, the investigation into precipitate coarsening kinetics was limited to a single temperature condition and a single composition of $Ni_{50}Ti_{40}Al_5Hf_5$. More recently, Hsu *et al.* [34] studied microstructural characteristics and properties of a wider composition range with a higher Hf concentration (20 at%). A series of compositions were investigated in order to systematically characterize the effect of small Al additions (0–5 at% Al) to $Ni_{50}Ti_{(30-X)}Hf_{20}Al_X$ alloys. The solubility limit of Al in the B2 $Ni_{50}Ti_{30}Hf_{20}$ matrix at 600 °C was experimentally determined to be 3 at%. Additionally, it was found that Al additions of $>$ 3 at% to $Ni_{50}Ti_{(30-X)}Hf_{20}Al_X$ led to the formation of Heusler phase on aging at 600 °C for 100 h. An increased concentration of Hf resulted in co-precipitation of the H-phase and Heusler phase precipitates, which was not observed by Jung et al. [29].

Therefore, it was surmised that Al and Hf additions to NiTi-based alloys will result in co-precipitation of both the Heusler and H-phase and achieve desirable strengthening while, under certain conditions, maintaining the transformation temperature within the range of 29–328 °C [34]. However, there are very limited studies on the microstructural evolution of the NiTiHfAl system upon aging. Therefore, characterizing the structural properties of this alloy could elucidate the effects of alloy design parameters on the formation of nanoscale coherent precipitates and ultimately establish reliable process-structure-property relationships. Thus, the purpose of this study is to investigate the evolution of the microstructure and Vicker's hardness in $Ni_{50}Ti_{21}Hf_{25}Al_4$ as a function of aging time at 600 °C.

2. Experimental

2.1. Alloy fabrication, processing and characterization

$Ni_{50}Ti_{21}Hf_{25}Al_4$ buttons were cast by arc melting 99.5 wt% Ni, 99.99 wt% Ti, 99.9 wt% Al, and 97.82 wt% Hf raw materials (Alfa Aesar) in an argon atmosphere. Samples were cast into 8 g and 70 g buttons on a water-cooled copper hearth and flipped six times between melts to ensure homogeneity.

The as-cast buttons were sealed in VakPak65 stainless steel bags for heat treatments. All samples were solution treated (ST) at 1050 °C for 100 h followed by oil-quenching, resulting in a homogenous matrix with a few interdendritic Hf-rich particles (Hf content $>$ 98 wt%), which remain undissolved after homogenization. Solution-treated material was then sectioned using a low-speed diamond saw and encapsulated in the evacuated quartz tubes ($<4 \times 10^{-2}$ Torr). Aging heat treatments were performed for 100 h at 600, 700 and 800 °C followed by oil-quenching. Additionally, samples were aged at 600 °C for 31, 70, and 1000 h. Heat treatments were selected based on previous literature [15,35–39] as well as Hsu *et al.* [34] study aiming for the co-precipitation of H-phase and Heusler. For the rest of this discussion, samples will be designated as ST/(Aging Temperature)/(Aging Time). For instance, the alloy ST/600 °C/100 h has been solution heat treated followed by aging at 600 °C for 100 h.

All of the samples were mounted in epoxy, ground down with 1200 grit SiC paper, and polished with alumina suspension (3 and 1 μm) followed by a 0.05 μm colloidal silica suspension. Hardness testing was performed on polished flat samples in a Tukon1102 Vickers hardness tester with a 1 kgf load and 10 seconds dwell time, following ASTM E92 [40]. Each data point is an average of seven measurements and the standard deviation represents 95 % standard error of the mean.

Powder x-ray diffraction (XRD) was performed to identify crystal structure using a Panalytical XPert Powder instrument with CuKα radiation in a 2θ range from 20 to 125 degrees and a step size of 0.008 degrees. All the samples were powdered using mortar and pestle. The XRD peaks were identified using PANalytical X'Pert HighScore Plus (v3.0) and cross-referenced against the database from Joint Committee on Powder Diffraction Standards.

For the microstructure characterization, SEM (TESCAN MIRA 3) was employed for precipitates identification and size measurement. Backscattered electron (BSE) mode was selected for SEM imaging to achieve composition-dependent image contrast. The samples for the SEM imaging were prepared using the same procedures as for the hardness measurement.

For high resolution observations and crystal structure determination, Transmission electron microscopy (TEM) imaging was conducted on a JEOL 2010F operating at an accelerating voltage of 200 kV. Samples for the TEM study were prepared by standard techniques [41] using a FEI Helios Nanolab 600 Dual Beam focused ion beam (FIB)-SEM. Selected area electron diffraction (SAED) patterns were collected for precise crystal structure determination of the precipitates. TEM with energy-dispersive X-ray spectroscopy (EDS) was employed for the elemental analysis while dark-field TEM imaging was performed to determine the size and morphology of the precipitates. High-angle annular dark-field (HAADF) imaging in STEM was performed on an aberration corrected Themis Z operated at an acceleration voltage of 200 kV with a convergence semi-angle of 25 mrad. To minimize the effect of scan distortions and sample drift during HAADF-STEM imaging, 20 images were sequentially recorded, rigidly aligned with a cross correlation method, and then averaged. In Themis, nanobeam electron diffraction pattern (NBED), with diameter condensed to 1.6 nm, was used for structural information on nanosized precipitates.

The SEM and TEM images were analyzed using the measurement tool available in Image J software [42] – an open-source platform renowned for its scientific image analysis capability, for the determination of precipitates dimensions and distribution within the samples. At least 20 different precipitates for each sample were measured and each reported value in this work represents an average of these measurements. The aspect ratio was calculated as length/width. The precipitates were isolated by employing a black and white contrast method, and the projected area fraction was subsequently calculated from two-dimensional images. For the microstructure characterization, SEM images were selected due to their wider field of view and improved statistical representation of the entire material. In case where SEM imaging was not practical due to a limited spatial resolution, HAADF-TEM images were used for the measurement of microstructure characteristics.

2.2. Precipitate coarsening behavior

The coarsening coefficient (k) for the H-phase precipitate at 600 °C was calculated from experimental precipitate size measurements using the classical Lifshitz-Slyozov-Wagner (LSW) coarsening theory of Ostwald ripening equation [43–45]:

$$r_t^3 - r_0^3 = kt \tag{1}$$

where r_t is the average radius of the particle at time t, r_0 is the initial average radius of the precipitates, and k is the coarsening coefficient. In the present study involving non-spherical particles, the average radius 'r' is derived from a volume-equivalent-ellipse.

2.3. Precipitation strengthening contribution prediction

The precipitation strengthening is attributed to the interaction between precipitates and dislocations through various mechanisms such as shearing, looping, or a combination of two mechanisms. The dominant strengthening mechanism depends on the precipitate size, morphology, and crystal structure. The contribution of the precipitation hardening mechanisms to the increase in strength of the aged alloys can be estimated by classical strengthening theories.

For instance, the precipitate order strengthening acts as the dominant strengthening mechanism when the dislocations interact with the anti-phase boundary and cut through a precipitate [46,47]:

$$\Delta\sigma_{ord} = \left(\frac{\sqrt{\gamma}}{b}\right)\left(\sqrt{\frac{4rf}{\pi T}}\right) \tag{2}$$

where γ is the antiphase boundary (APB) energy (0.5 J/mm) of (111) slip planes in the B2 NiTi [48], b is the magnitude of the Burger's vector in $\pm <001>$ (b=0.15) [49], f is the volume fraction of the precipitate that was estimated using the area fraction of the precipitate according to the high-resolution TEM (HRTEM) and BSE/SEM images, and T is the temperature.

When a dislocation bows between two precipitates, the increase in alloy strength is described as the Orowan strengthening mechanism:

$$\Delta\sigma_{0.2} = \frac{Gb}{L} \tag{3}$$

where G is the shear modulus of the austenitic NiTi as 80 GPa [50], L is the interparticle spacing estimated based on Törrönen's equation [51]:

$$L = \beta\left(\frac{N_A r}{h+r}\right)^{-1/2} - r \tag{4}$$

where β is a measure of the randomness of particle distribution (assumed as Törrönen to be a constant = 1.23), N_A is the number of particles per unit area (obtained from HRTEM images), r is the equivalent radius for non-spherical precipitate in this study, and h is the foil thickness which was measured equal to 50 nm (thickness of the TEM lamella extracted and measured by FIB-SEM).

3. Results

3.1. Effect of aging temperature and time on mechanical properties

Fig. 1(a) shows the effect of aging temperature on microhardness via isochronal aging treatment performed for 100 h. The hardness of the solution-treated alloy is 572 ± 12 HV. After 100 h of aging at 600 °C, the hardness increases to 722 ± 12 HV, an increase of ~25 % over the solution-treated alloy. After 100 h of aging at 700 °C and 800 °C, a decrease in hardness compared to solution-treated alloys is observed, reaching values as low as 467 ± 12 HV.

Since the highest hardness value of 722 ± 12 HV is obtained upon aging at 600 °C, this condition has been chosen for subsequent investigation. Fig. 1(b) shows the effect of isothermal aging time on hardness at 600 °C. Peak hardness of 756 ± 5 HV is achieved on aging for 70 h, an increase of approximately 30 % over the solution-treated samples. On further aging at 600 °C up to 1000 h, the hardness of the alloy slightly decreases to 672 ± 18 HV, a drop of approximately 11 % from peak hardness.

3.2. Microstructural characterization

XRD was conducted on the ST sample and samples aged for 31, 70, 100, and 1000 h at 600 °C, revealing the presence of the following phases: B2 austenite, B19' martensite, Ti_2Ni-type phase, Ni_2TiAl Heusler, and H-phase, as seen in Fig. 2. The matrix was identified as primarily B2 austenite. Ti_2Ni-type peaks are observed in the samples aged from 70 h to 1000 h, as it is a commonly occurring phase in most NiTi-based alloys [52,53]**.** The diffraction peaks associated with the H-phase were indexed according to the literature [15,54]. A Heusler phase peak was detected in the XRD spectra of the overaged sample (1000 h) of $Ni_{50}Ti_{21}Hf_{25}Al_4$ alloy, likely due to its increased size and volume fraction under that specific aging condition.

Fig. 3 shows a BSE/SEM image of the ST/600 °C/70 h sample exhibiting the highest hardness value. The image shows numerous uniformly distributed elongated precipitates with a higher intensity, indicating that they are enriched in heavy element, i.e., Hf. These precipitates have an average length of 45 ± 6 nm and a width of 18 ± 3 nm. The longer axis of these precipitates is notably aligned orthogonally, indicating at least two preferential precipitation orientations. Hf-rich precipitates with a similar lenticular morphology and size (40–80 nm in length and 20–40 nm in width after being aged for 100 h at 600 °C) have been identified as the H-phase precipitates in $Ni_{50.1}Ti_{24.9}Hf_{25}$ [13,14,22,26,44]. H-phase precipitates in the alloy studied in this work are

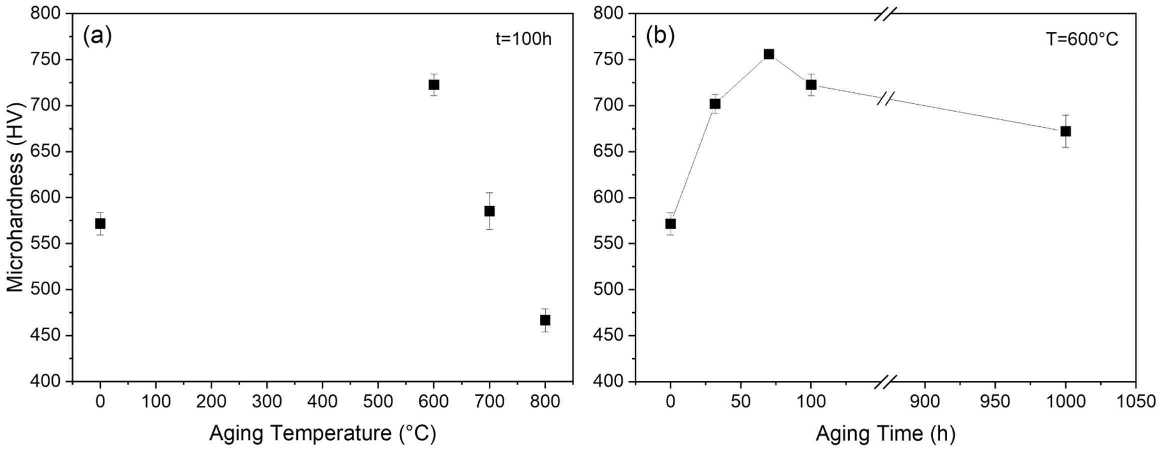

Fig. 1. Vickers micro hardness as a function of (a) aging temperature on sample for 100 h and (b) aging time for an aging temperature at 600 °C.

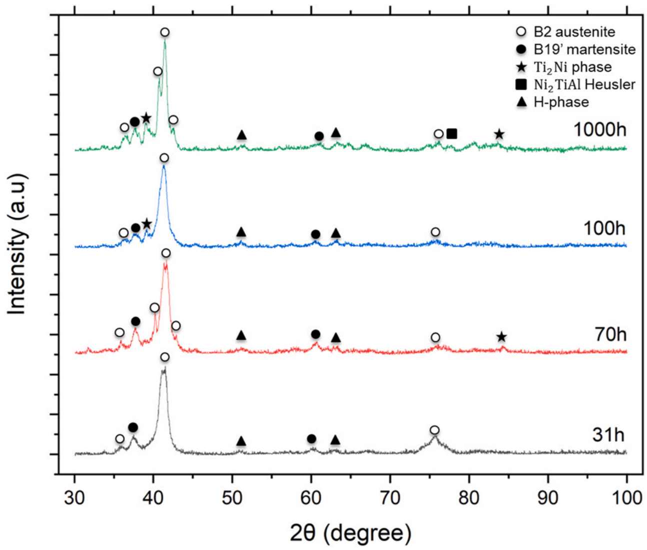

Fig. 2. XRD spectra of ST/600 °C/31 h, ST/600 °C/70 h, ST/600 °C/100 h, ST/600 °C/1000 h samples.

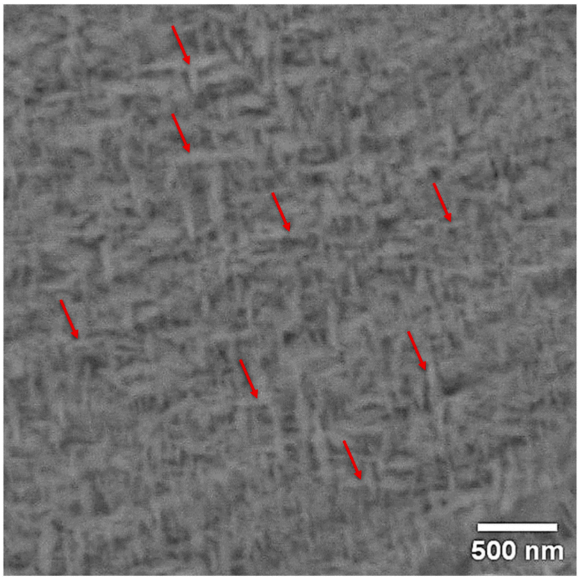

Fig. 3. SEM backscatter electron mode image of sample ST/600 °C/70 h at peak hardness showing the lenticular H-phase precipitates marked with red arrows.

confirmed by the TEM analysis which will be further discussed.

TEM studies were conducted to obtain crystal structure information of the phases formed in this alloy after ST and various aging times at 600 °C (31, 70, 100, 1000 h). Fig. 4(a) shows the SAED pattern of the ST sample recorded along the [011] zone axis and the primary reflections, depicted by yellow circles are consistent with the B2 matrix. Fig. 4(b) shows the diffraction pattern of the ST/600 °C/31 h sample recorded along the [011] zone axis. The reflections marked with yellow circles are consistent with the B2 matrix while those reflections, labeled with red arrows, correspond to the H-phase precipitates [14,26]. The diffraction spots marked with blue arrows are consistent with the Heusler phase precipitates [12,29,34], still, these reflections arise from both H-phase and Heusler along the same zone axis [26]. According to the literature [29], Heusler phase has been previously investigated using electron diffraction along the [011] or [112] zone axis. However, the high tilting angle makes it challenging to have access to the [112] zone axis for the same sample location. Therefore, the identification of Heusler phase via SAED in the presence of H-phase along [112] was not conducted in this work. Additionally, after aging for 31 h, the Heusler phase precipitates were found to be closely-spaced and in early stages of ordering [34]. To the authors' knowledge, due to the difficult in detecting Heusler phase via TEM at such early aging time at 600 °C, no other study on a similar alloy has been able to resolve that precipitate phase. Hsu *et al.* [34] used atom probe tomography (APT) which eliminates the projection effect by reconstructing element distribution in three dimensions. Later, Jung *et al.* [12] studied more coarsened precipitates obtained after aging up to 1000 h at a composition that did not engender interference from any other precipitate. Therefore, due to the higher likelihood of identifying distinct phases, the SAED patterns with longer aging time, 100 h, are presented in Fig. 4(c) and (d). Due to their specificities, TEM results for samples aged for 70 h and 1000 h will be detailed further.

Fig. 4(c) and (d) show the SAED patterns of the ST/600 °C/100 h along [011] and [001] projections with respect to the B2 matrix, respectively. The pattern is indexed with respect to the B2 matrix as indicated by the yellow markings. The blue arrows in Fig. 4(b) and (c) highlight reflections that are consistent with the L2$_1$ Ni$_2$TiAl Heusler phase [12]. The characteristic H-phase reflections in Fig. 4 are indicated by the red arrows [13,26,55].

Fig. 5(a) shows a HAADF-STEM image of the ST/600 C/70 h sample along the $[0\overline{3}\overline{1}]_H[0\overline{1}0]_{B2}$ zone axes, where the subscripts represent the H-phase and B2 structure, respectively. Lenticular precipitates were observed with their length ranging in the 40–50 nm. These precipitates show two preferential growth directions along $[100]_{B2}$ and $[001]_{B2}$ Shown in Fig. 5(b) is a magnified atomic-resolution HAADF-STEM image of the yellow boxed region in Fig. 5(a), demonstrating the coherency between the precipitate and matrix. Note that as the intensity of HAADF-STEM images is sensitive to atomic number (Z), the heavy Hf atoms (Z = 72) appear brighter than the light Ni and Ti atoms (Z = 28 and 22, respectively). Thus, the bright regions in Fig. 5(b) represent the H-phase precipitate. The fast Fourier transformation (FFT) of this region in Fig. 5(c) confirms the previously described preferential precipitate growth directions ($[100]_{B2}$ and $[001]_{B2}$) The lenticular oblate morphology of the H-phase precipitates and their orientation relation with the matrix are consistent with the observations reported in the literature [6,14,26,34,55]. The Heusler precipitates are known to be spherical or cuboidal in morphology and to be smaller than 10 nm in $Ni_{50}Ti_{21}Hf_{25}Al_4$ after being aged for 100 h at 600 °C [11,13]. In the HAADF-STEM images, no Heusler precipitates were observed. This is partially because HAADF-STEM imaging is not very sensitive to small amounts of light element atoms such as Al (Z = 13) when they are present with heavier elements. Several large H-phase precipitates were found in the sample which were considered nucleated during aging [56].

The length, aspect ratio and interspacing evolution of the H-phase precipitate at steps of 31, 70, 100 and 1000 hwere summarized in Table 1, measured from SEM images. H-phase precipitates with an average length of 33 ± 4 nm and an interspacing of 21 nm were found in the sample after 31 h of aging. After 70 h of aging, there is a significant increase in the precipitate length increases to 45 ± 6 nm, in addition to an increase in the interparticle spacing to 27 nm. As the alloy undergoes extended aging, up to 100 h and 1000 h, the precipitate length increases to 55 ± 3 nm and 114 ± 11 nm respectively, as well as interparticle spacing increases from 29 ± 7–36 ± 10 nm, presenting the same aspect ratio. The equivalent spherical radius of the H-phase precipitate was obtained using the conversion of the ellipsoid.

Shown in Fig. 6 is a dark-field TEM image of sample ST/600 C/70 h, that exhibits peak hardness, revealing precipitates of varying contrast with lenticular and spherical/cuboidal morphology. Opposingly to the lenticular precipitates, previously determined as H-phase in this work, Heusler precipitates were found to be spherical at similar aging conditions and coarsen to cuboidal precipitates [34]. Therefore, it is expected that the spherical/cuboidal shaped precipitates observed in Fig. 6 are

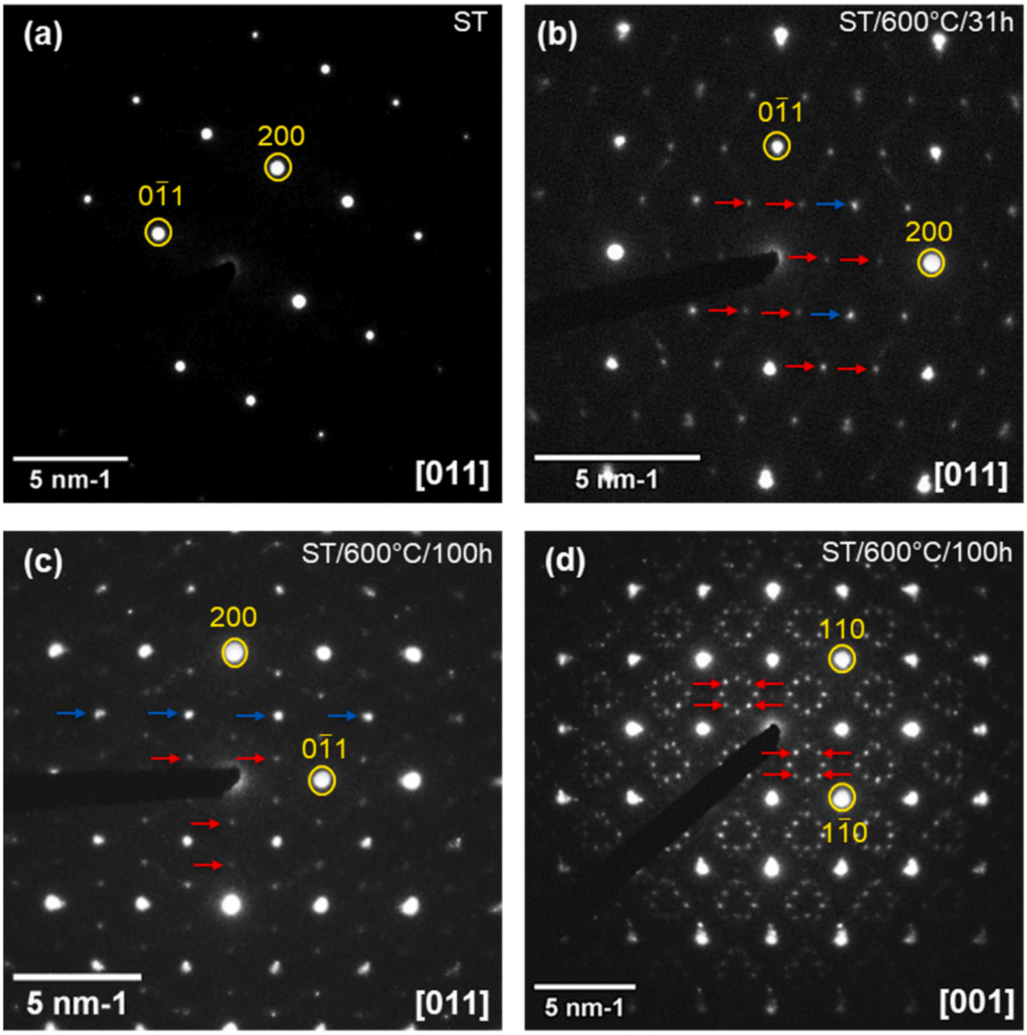

Fig. 4. SAED patterns from the: (a) ST alloy; (b) ST/600 °C/31 h alloy; (c) and (d) relate to ST/600 °C/100 h alloy. Respective zone axis is indicated in each SAED pattern. B2 matrix reflections are labeled with yellow circles, H-phase reflections are indicated by red arrows and Heusler phase reflections are indicated by blue arrows.

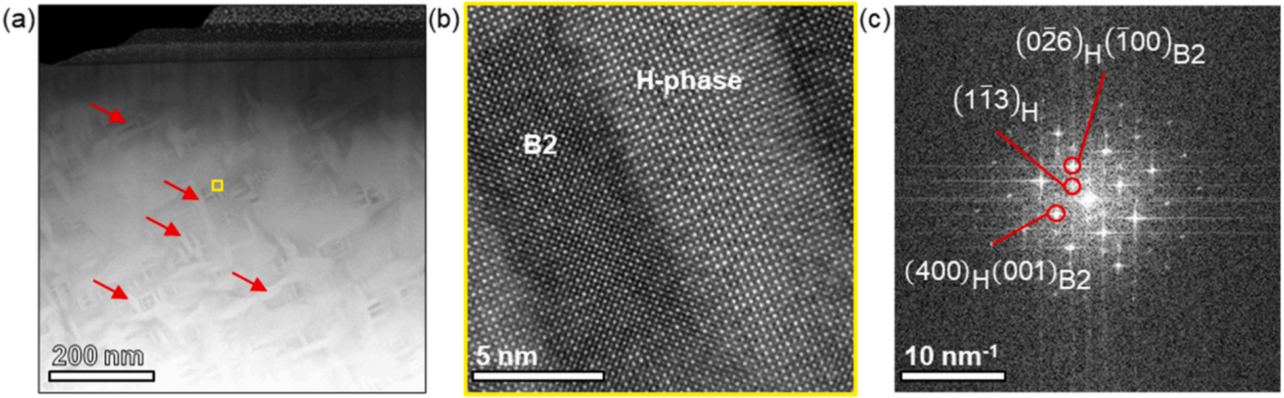

Fig. 5. HAADF-STEM images of (a) the ST/600 °C/70 h sample showing H-phase precipitates labeled with red arrows; (b) a magnified region from the yellow box in (a) showing the coherent interface between the H-phase precipitate and the B2 matrix. HAADF-STEM imaging is sensitive to atomic numbers causing the Hf-rich precipitates to appear brighter than the matrix. Analysis on (c) the corresponding fast Fourier transform (FFT) of the area in (b) confirms the orientation relationships of $[0\overline{31}]_H[0\bar{1}0]_{B2.}$

Heusler precipitates. We note that two overlapping precipitates can be observed as a diffuse halo around a bright contrast precipitate. The projection effect is highlighted when observing the atom probe tomography reconstruction in Hsu *et al.*'s study [34] where it is possible to resolve individual Heusler phase precipitates in the three dimensional reconstruction. Therefore, in centered dark-field images in Fig. 6,

Table 1
Average particle length, aspect ratio, and interparticle spacing of the H-phase, measured from SEM images. Average particle radius of the Heusler phase in the Ni50Ti21Hf25Al4 alloy, which underwent solution heat treated at 1050 ℃ for 100 h and aged at 600 ℃ for different times. The measurements for Heusler precipitates were obtained from high resolution TEM images.

	H-phase					Heusler
Sample	Particle Length (nm)	Aspect Ratio	Equivalent Spherical Radius (nm)	Interparticle Spacing (nm)	Volume fraction (%)	Particle radius (nm)
ST/600 °C/31 h	33 ± 4	2.4 ± 0.4	18 ± 4	21 ± 7	16 ± 2	-
ST/600 °C/70 h	45 ± 6	2.5 ± 0.6	24 ± 3	27 ± 8	22 ± 2	10 ± 1
ST/600 °C/100 h	55 ± 3	3.0 ± 0.2	26 ± 1	29 ± 7	25 ± 3	-
ST/600 °C/1000 h	114 ± 11	3.1 ± 0.6	36 ± 4	36 ± 10	26 ± 1	28 ± 4

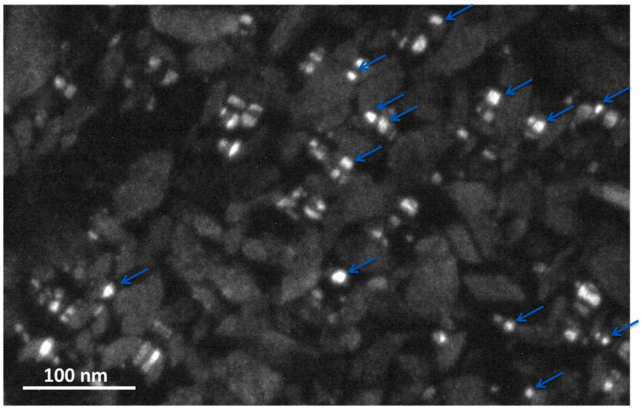

Fig. 6. Centered dark-field TEM image of ST/600 °C/70 h obtained using the (111) reflection. Bright spherical/cuboidal precipitates represent the Heusler phase and are labeled with blue arrows.

obtained using the (111) matrix reflection, precipitates which are spherical/cuboidal and have a bright contrast without a halo are accounted and measured for particle size (labeled with blue arrows). This resulted in an average radius of 10 ± 1 nm (Table 1), measured from high resolution TEM images, a size range that is consistent with that observed in other studies [12,34].

Fig. 7(a) shows the HAADF-STEM image of $Ni_{50}Ti_{21}Hf_{25}Al_4$ alloy with the extended aging condition, i.e., ST/600 °C/1000 h. The atomic-number sensitive image contrast reveals two distinct regions with high and low image intensities: (i) bright, lenticular shaped H-phase and (ii) dark, Al enriched area. Shown in Fig. 7(b) and (c) are the corresponding EDS elemental maps of Al and Hf, indicating the potential locations of the spherical/ellipsoidal Heusler precipitates and the H-phase precipitates. This result shows that extended aging leads to a change in morphology of Al-containing Heusler phase precipitates from cuboidal/spherical to spherical/ellipsoidal with the precipitation's average size being 28 ± 4 nm (Table 1). Area fraction was estimated from the 2D projections of the HAADF-STEM images for the overaged sample ST/600 °C/1000 h, and Heusler represents approximately 2.2 %, whereas H-phase corresponds to more than 55 % in area.

Fig. 8(a) and (b) show the HAADF-STEM images of the ST/600 ℃/1000 h sample, where (b) shows the magnified image from the yellow box in (a), revealing two precipitates identified as H-phase (TiHf)Ni and $L2_1$ Heusler precipitates Ni_2TiAl. Fig. 8(c) displays a NBED pattern collected in the dark image-intensity region, showing the Heusler phase reflections (labeled with yellow) along the [110] projection. Note that the electron beam used for NBED acquisition is condensed down to a diameter of 1.6 nm (full width at half maximum), allowing for isolating diffraction signal from targeted locations. In this case, the beam was positioned right at the Al-rich Heusler region. Fig. 8(d) and (e) are EDS maps of Al and Hf in yellow and green, respectively, evidencing the Al-rich Heusler phase and the Hf-rich H-phase.

4. Discussion

4.1. Microstructural evolution

$Ni_{50}Ti_{21}Hf_{25}Al_4$ alloy reached its peak hardness following a 70 h aging process at 600 °C. Under this condition, the alloy has H-phase and Heusler precipitates with dimensions of 45 ± 6 nm (length) and 10 ± 2 (diameter) nm, respectively (Table 1). The size evolution of H-phase was traced as a function of aging time. The size of Heusler precipitates observed in this work is similar to that observed by Hsu *et al.* using atom probe tomography [34].

In the peak aged alloy (ST/600 °C/70 h), most precipitate strengthening contribution is expected from both H-phase and Heusler precipitates combined. The length of interspacing spacing of H-phase precipitates increase from 45 ± 6 nm and 27 ± 8 nm (aging 70 h) to

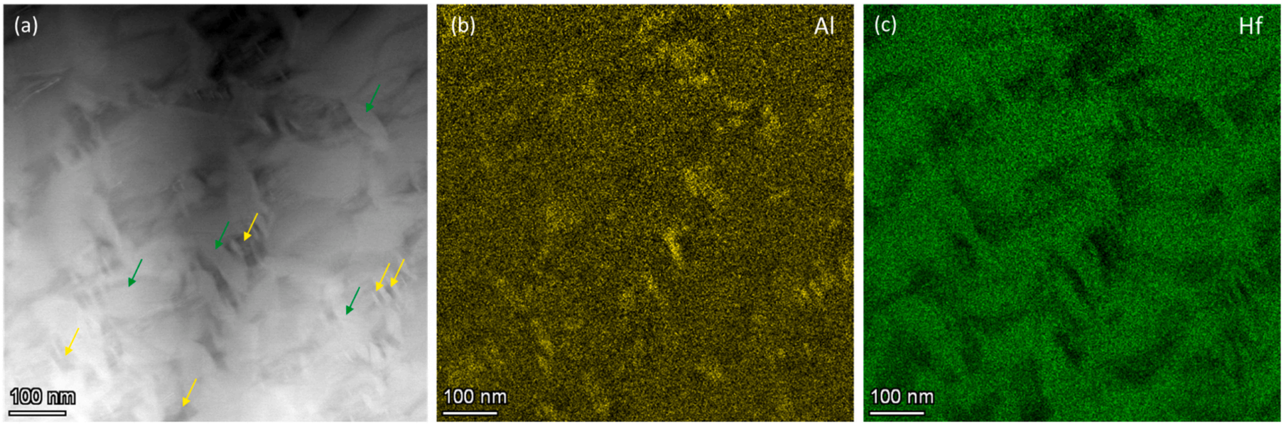

Fig. 7. (a) HAADF-STEM image the ST/600 °C/1000 h sample with two different precipitates labeled with green and yellow arrows; (b) EDS map showing Al-rich areas in yellow, indicating potential sites of Ni_2TiAl precipitates in (a); (c) EDS map showing Hf-rich areas in green, corresponding to the lenticular H-phase precipitates in (a).

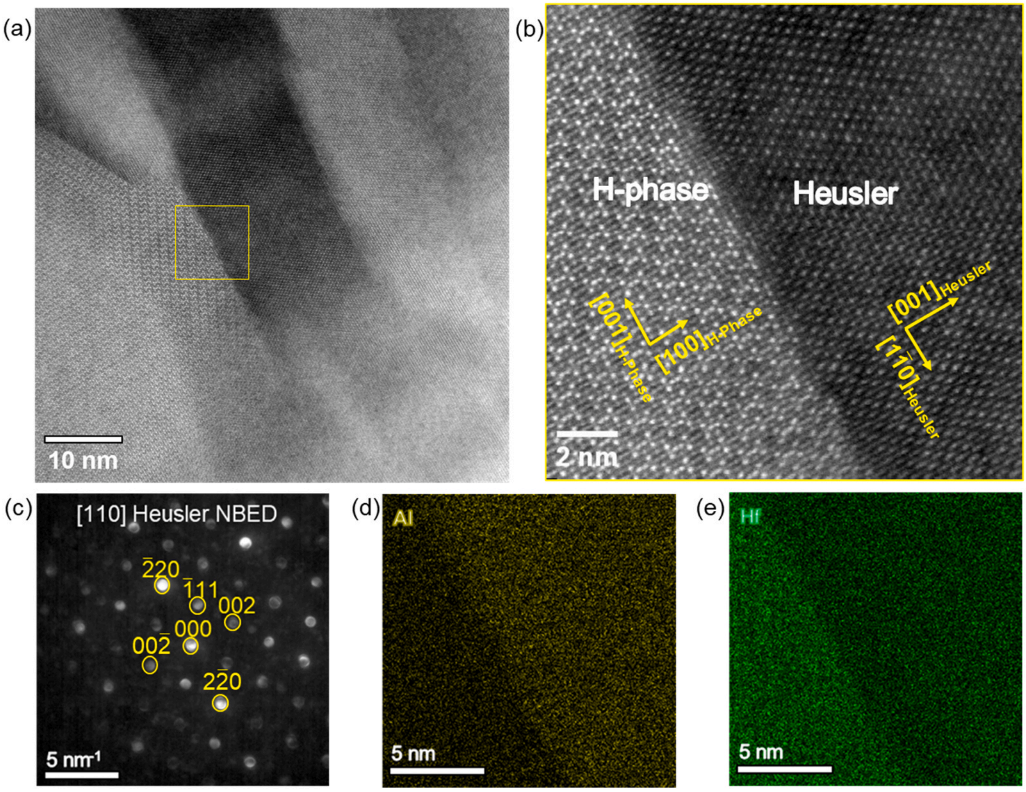

Fig. 8. (a) HAADF-STEM image the ST/600 °C/1000 h sample; (b) a magnified region from the red box in (a) showing the interface between two precipitates identified as H-phase (TiHf)Ni and $L2_1$ Heusler precipitates Ni_2TiAl. The zone axis for the H-phase in (b) is [010]. In (c) a NBED taken from the [110] zone axis, showing the Heusler phase reflections (labeled in yellow). (d) and (e) are EDS maps of Al and Hf in yellow and green, respectively.

114 ± 11 nm and 36 ± 10 nm, respectively, after aging for 1000 h (Table 1). This increase in precipitate size and interparticle spacing, along with an increase in hardness up to 70 h followed by a sharp drop in hardness upon aging beyond 70 h, indicates onset of over aging after 70 h.

Regarding the Heusler precipitates evolution, we observe the increase in radius from 10 ± 1 nm after 70 h of aging to 28 ± 4 nm after 1000 h of aging (Table 1), as well as a slight change in morphology, from a cuboidal/spherical to a spherical/ellipsoidal. The area fraction of the Heusler phase in the overaged condition (ST/600 °C/1000 h) was estimated to be approximately 2.2 %. Based on the pseudo-ternary diagram provided by Hsu *et al.* [34] for the same system aged at 600 °C for 100 h, by applying the lever rule, calculations predict a volume fraction of around 4 % of Heusler in the B2 matrix for a shorter aging time. This discrepancy could arise various factors, including the limited sampling areas examined in TEM, which may result in an uneven distribution of Heusler precipitates. However, due to the inability to observe the Heusler phase in broader areas using SEM, the measurements were performed using the HAADF-STEM images.

Using the experimentally obtained H-phase precipitate size (Table 1), the coarsening kinetics of the spherical-equivalent H-phase at 600 °C was investigated. The precipitate radius evolution of $\left(r_t^3 - r_0^3\right)$ as a function of the aging time is plotted in Fig. 9 according to Eq. 1, using the classical LSW theory.

A two-stage coarsening behavior can be observed in the plot. The plotted results suggest a slope change in the linear fitting at between 70 h to 100 h, when coarsening rate decelerates. According to the LSW theory, the slope of the fitting line is the coarsening coefficient (k) of the H-phase. Thus, it is possible to estimate the two-stage coarsening coefficients, k_1 and k_2, to be 4.9×10^{-2} nm^3/s up to approximately 70 h of aging, and $0.9 \text{ x } 10^{-2}$ nm^3/s for longer aging times. The literature review [57–59] highlights that the coarsening kinetics of the primary precipitate can be affected by the precipitation of a secondary phase. Therefore, a two-stage coarsening behavior may occur in multi-element alloy systems. That is in consonance with the findings of the present work, where Heusler phase was observed in the alloy aged for 70 h and longer. It indicates that the coarsening behavior of H-phase was affected by the presence of Heusler in the alloy's mucrostructure, resulting in a

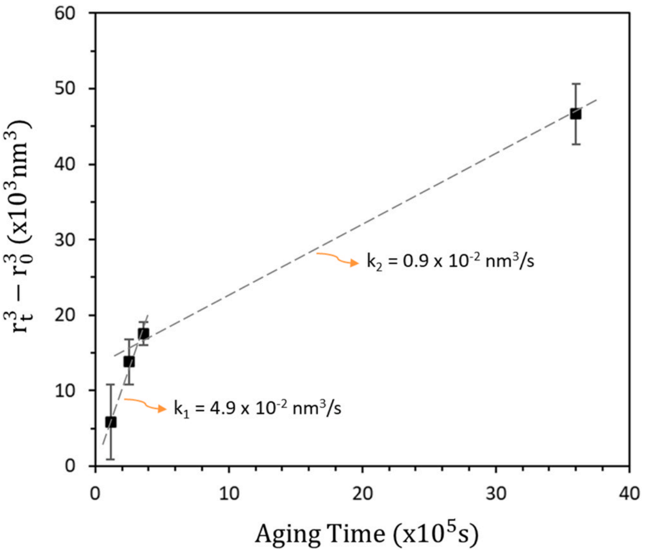

Fig. 9. LSW analysis of the size evolution of the H-phase particles measured by the TEM, as a function of aging time up to 1000 h at 600 °C. A two-stage coarsening rate can be observed. The coarsening coefficients k_1 and k_2 were determined by the slope of the fitting curves. R-square value is over 0.98, showing a good linear fitting.

significantly lower coarsening coefficient.

The experimental coarsening coefficient of H-phase in the NiTiHfAl system aged for 70 h and up at 600 °C is similar to that calculated for γ'' in INCONEL 718™ alloy (1.1×10^{-2} nm^3/s at 700 °C) [60] and is a few orders of magnitude smaller than the coarsening rate coefficient of γ' in some Ni-based superalloys, such as NIMONIC 115 (4.9×10^2 nm^3/s at 750 °C) [61] in a similar temperature range.

Since the size evolution of Heusler phase precipitates could not be traced at each aging step, the kinetics of the Heusler phase in $Ni_{50}Ti_{21}Al_4Hf_{25}$ could not be determined in this study. However, Heusler phase is known to follow coarsening kinetics at 600 °C in a $Ni_{50}Ti_{40}Al_5Hf_5$ alloy [12], which resonates with the precipitate sizes measured using dark-field TEM (ST/600 °C/70 h) and HAADF-STEM (ST/600 °C/1000 h). Jung *et al.* [12] found that the Heusler phase might quickly reach the coarsening stage after nucleation in the $Ni_{50}Ti_{40}Al_5Hf_5$ alloy. This observation is reasonable according to the measured hardness change shown in Fig. 1(b) in this study, which shows single peak hardness with two kinds of precipitates contributing to strengthening.

For this alloy, aging more than 70 h leads to the Heusler phase being smaller in size compared to H-phase. This result is consistent with the findings reported by Hsu *et al.* [34].

4.2. Mechanical behavior

While several hardening mechanisms may be acting concomitantly in this multicomponent system, the contribution of the co-precipitation of the H-phase and Heusler phase likely dominate. The contribution of H-phase to the strength increase (Δσ) of the alloy was estimated as a function of equivalent precipitate radius, according to Eqs. 2 and 3, at each aging step. This contribution is plotted in Fig. 10, where the blue line is related to the order strengthening mechanism and the green line is related to the Orowan strengthening mechanism.

The measured microhardness was converted into strength using a 3:1 conversion to be compared with the prediction values [62]. Fig. 10 shows data points (black squares) related to the experimentally measured strength change values (Δσ) compared to the ST sample, taken as reference (red circle).

According to the predictions plotted in Fig. 10, the dominant strengthening mechanism will change from order strengthening to Orowan, when the equivalent precipitate radius grows larger than ~25 nm. Thus, the H-phase contribution to the alloy strengthening can be inferred as order strengthening at steps of 31 and 70 h (blue line), then switched to Orowan strengthening at steps of 100 h and after (green line).

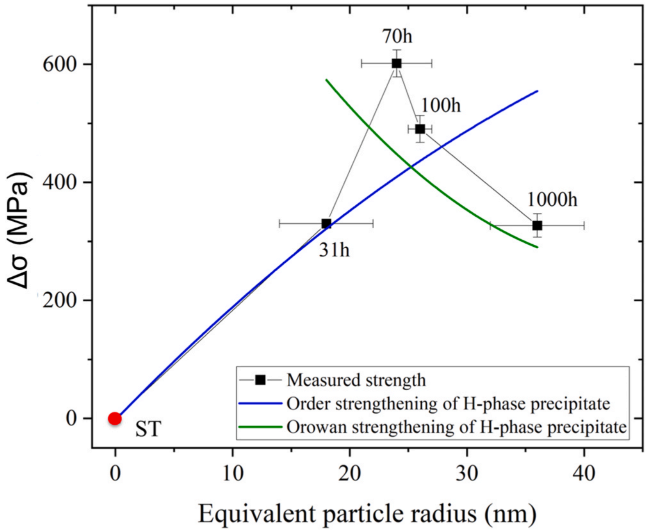

Fig. 10. Predicted order (blue line) and Orowan (green line) strengthening contribution of H-phase precipitate at aging steps of ST/600 °C/31 h, ST/600 °C/70 h, ST/600 °C/100 h and ST/600 °C/1000 h. The corresponding experimentally measured strength increase (Δσ) is plotted in black squares. Sample ST (reference value) is marked with red circle.

A significant additional increment in the experimental data (black squares) compared to the predictive models (blue and green lines) can be observed. The difference between the experimental data points (black squares) and predictive curves (blue and green lines) refers to the additional contribution of other strengthening mechanisms, whereas the predictions accounted for the H-phase precipitate contribution singularly. It can be inferred that it is related to the contribution from the nanoscale coherent Heusler phase precipitation strengthening. Therefore, the strength increase (Δσ) in the $Ni_{50}Ti_{21}Al_4Hf_{25}$ alloy after aging should be a result of the combined contribution from both H-phase and Heusler precipitates, achieving a peak hardness after 70 h of aging.

This assumption was supported by the observation that the H-phase precipitates are coherent with the matrix in the ST/600°C/70 h sample (Fig. 5). The order strengthening usually occur when the precipitate is coherent or semi-coherent [63]. With the absence of the Heusler precipitate size evolution at each step, the strengthening contribution from the Heusler precipitate could not be calculated. However, it is possible to observe the difference between the measured strength increase plotted in Fig. 10 (black squares) and the predicted strength (green and blue lines), theoretically calculated using Eqs. 2 and 3 accounting only for the H-phase contribution.

It is worth noting that the blue line, that accounts for the order strenghtening contribution from H-phase, aligns well with experimental data up until 31 h of aging. Analouglously, at the early stages of aging, Hsu *et al.* claimed that the Heusler precipitates were closely-spaced and in early stages of ordering [34].

Upon aging above 31 h the Heusler phase seems plays a significant role in the strength increase contribution to the system. The difference between the experimental peak hardness condition (ST/600 °C/70 h) and the predicted curve intersection is of approximately 150 MPa. Furthermore, the contribution of Heusler is reduced upon aging for 100 h and 1000 h, but still noteworthy.

Aging for 70 h produces an optimal combination of Heusler particle size and H-phase, and it is possible to assume that the increase is due to the theoretical particle shearing model for Heusler phase, with a 10 nm diameter. Bender and Olson [64] studied the strengthening effect of Heusler precipitates in a NiTiZrAl alloy. They predicted both shear and Orowan strengthening mechanisms for Heusler, and found out an optimal particle diameter of 3.1 nm after aging for 10 h at 600 °C. Therefore, it is reasonable to infer that the predominant strengthening mechanism provided by the Heusler precipitates is order strengthening at steps of 31 h and 70 h, then switched to Orowan strengthening upon aging for 100 h and above. Nevertheless, further investigation is needed.

The Vickers hardness of the ST/600 °C/70 h alloy shows that this quaternary system is promising for high-strength and high-hardness applications. In order to provide a context to the hardness measurements, Fig. 11 shows hardness values for various alloys. The peak hardness of $Ni_{50}Ti_{21}Hf_{25}Al_4$ alloy aged for 70 h at 600 °C, 756 ± 5 HV, is higher than several NiTi-based alloys, in grey [10,13–17,39,54,65]. The 55Ni-37Ti-8Al alloy, studied by Chen *et al.* [35], presented superior hardness value (820 HV) after aging at 400°C for 3 h. The authors [35] atributed this result to the refinement of the primary strengthening phase Ni_4Ti_3 and the precipitation of Ni_2TiAl phase owed to the 8 at% of Al addition. Jung *et al.* [29] previously investigated a 50Ni-45Ti-5Al aged alloy and also identified the presence of Heusler Ni_2TiAl phase, even though they didn't assess alloy's hardness.

5. Conclusions

The present work focused on the effects of aging heat treatments on the microstructure and mechanical properties of the quaternary

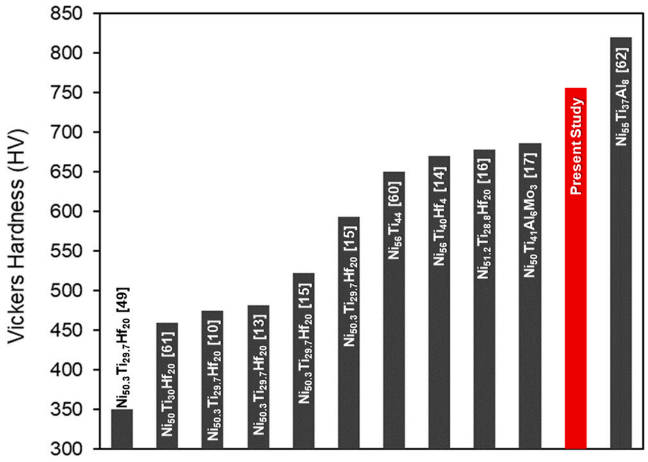

Fig. 11. Vickers hardness of $Ni_{25}Ti_{21}Hf_{25}Al_4$ (present study, red) in the peak hardness condition (ST/600 °C/70 h), compared with other NiTi-based alloys (dark gray).

NiTiHfAl system. Conclusions are summarized below:

1. Precipitation of nanoscale coherent $L2_1$ Heusler phase and face-centered orthorhombic H-phase was observed in the $Ni_{50}Ti_{21}Hf_{25}Al_4$ alloy aged at 600 °C. Two preferential growth orientations of H-phase precipitates were indicated along $[-100]_{B2}$ and $[0,1]_{B2}$. The precipitate size and number density of H-phase precipitates were reported at each aging step.
2. Heusler nanoprecipitates were characterized after 1000 h of over aging, evidencing a slight morphology change from cuboidal/spherical to spherical/ellipsoidal, and the particles' average dimension increase from 10 ± 1 nm, after 70 h of aging, to 28 ± 4 nm, after 1000 h of aging.
3. The peak hardness condition of 756 ± 5 HV was achieved after solution treatment at 1050 °C for 100 h followed by aging at 600 °C for 70 h. This is a promising result for high strength and high wear resistance applications, such as bearing, actuators and other tribological parts.
4. The coarsening kinetics of the primary H-phase precipitates was affected by the precipitation of Heusler phase above 70 h of aging at 600 °C. A two-stage coarsening behavior was observed, whereas the coarsening coefficients k_1 (up to 70 h of aging) and k_2 (above 70 h of aging) of the H-phase phase could be estimated as 4.8×10^{-2} nm^3/s and 0.9×10^{-2} nm^3/s, respectively.
5. There is a combined strengthening effect accounted for both precipitates after aging the $Ni_{50}Ti_{21}Hf_{25}Al_4$ alloy: H-phase and Heusler. From the difference between the experimentally measured increase in strength and the calculated theoretical strengthening accounting for the H-phase contribution only, Heusler plays a significant role specially in the peak hardness condition (ST/600 °C/70 h).

CRediT authorship contribution statement

Flavia da Cruz Gallo: Writing – original draft, Visualization, Validation, Methodology, Investigation, Formal analysis, Data curation. **Hunter B. Henderson:** Validation, Formal analysis, Data curation. **Monica Kapoor:** Writing – review & editing, Validation, Supervision, Formal analysis, Data curation. **Eitan Hershkovitz:** Validation, Software, Data curation. **Yang Yang:** Writing – review & editing, Visualization, Validation, Data curation. **Honggyu Kim:** Writing – review & editing, Validation, Supervision, Resources, Project administration, Funding acquisition. **Michael S. Kesler:** Writing – review & editing, Visualization, Validation, Supervision, Methodology, Data curation. **Michele V. Manuel:** Writing – review & editing, Validation, Supervision, Resources, Project administration, Funding acquisition, Conceptualization.

Declaration of Competing Interest

The authors declare that they have no known competing financial interests or personal relationships that could have appeared to influence the work reported in this paper.

Acknowledgments

This work was conducted in part at the Research Service Centers of the Herbert Wertheim College of Engineering at the University of Florida with the valuable assistance of Dr. Nicholas Rudawski. The research was supported by a National Aeronautics and Space Administration Early Career Faculty Award no. NNX12AQ42G and National Science Foundation (Award No. 2226478) from the Metals and Metallic Nanostructures Program within the Division of Materials Research.

Data Availability

Data will be made available on request.

References

[1] C. Dellacorte, R.D. Noebe, M.K. Stanford, S. a PadulaResilient and corrosion-proof rolling element bearings made from superelastic Ni-Ti alloys for aerospace mechanism applications, Nasa Tm2011, 143166021710510.1520/STP103887.

[2] C. Dellacorte, W.A. Wozniak, Design and Manufacturing Considerations for Shockproof and Corrosion-Immune Superelastic Nickel-Titanium Bearings for a Space Station Application, (2012).

[3] J. Mohd Jani, M. Leary, A. Subic, M.A. Gibson, A review of shape memory alloy research, applications and opportunities, Mater. Des. (1980-2015) 56 (2014) 1078–1113, https://doi.org/10.1016/j.matdes.2013.11.084.

[4] S. Jiang, Y. Zhao, Y. Zhang, L. Hu, Y. Liang, Effect of solution treatment and aging on microstructural evolution and mechanical behavior of NiTi shape memory alloy, Trans. Nonferrous Met. Soc. China 23 (2013) 3658–3667, https://doi.org/10.1016/S1003-6326(13)62914-3.

[5] H.E. Karaca, S.M. Saghaian, G. Ded, H. Tobe, B. Basaran, H.J. Maier, R.D. Noebe, Y.I. Chumlyakov, Effects of nanoprecipitation on the shape memory and material properties of an Ni-rich NiTiHf high temperature shape memory alloy, Acta Mater. 61 (2013) 7422–7431, https://doi.org/10.1016/j.actamat.2013.08.048.

[6] F. Yang, D.R. Coughlin, P.J. Phillips, L. Yang, A. Devaraj, L. Kovarik, R.D. Noebe, M.J. Mills, Structure analysis of a precipitate phase in an Ni-rich high-temperature NiTiHf shape memory alloy, Acta Mater. 61 (2013) 3335–3346, https://doi.org/10.1016/j.actamat.2013.02.023.

[7] S.F. Hsieh, S.K. Wu, H.C. Lin, C.H. Yang, Transformation sequence and second phases in ternary Ti–Ni–W shape memory alloys with less than 2 at% W, J. Alloy. Compd. 387 (2005) 121–127, https://doi.org/10.1016/j.jallcom.2004.06.026.

[8] K. Wada, Y. Liu, Shape recovery of NiTi shape memory alloy under various prestrain and constraint conditions, Smart Mater. Struct. 14 (2005) S273–S286, https://doi.org/10.1088/0964-1726/14/5/016.

[9] N. Ono, A. Tsukahara, R. Kainuma, K. Ishida, The properties of two-phase Ni–Al–Fe shape memory alloys in the virgin and shape-memory-cycled states, Mater. Sci. Eng. A 273–275 (1999) 420–424, https://doi.org/10.1016/S0921-5093(99)00310-X.

[10] H.E. Karaca, E. Acar, H. Tobe, S.M. Saghaian, NiTiHf-based shape memory alloys, Mater. Sci. Technol. 30 (2014) 1530–1544, https://doi.org/10.1179/1743284714Y.0000000598.

[11] Y. Wang Chai, Y. Kimura, Nanosized precipitates in half-Heusler TiNiSn alloy, Appl. Phys. Lett. 100 (2012) 033114, https://doi.org/10.1063/1.3679377.

[12] J. Jung, G. Ghosh, G.B. Olson, A comparative study of precipitation behavior of Heusler phase (Ni 2TiAl) from B2-TiNi in Ni-Ti-Al and Ni-Ti-Al-X (X = Hf, Pd, Pt, Zr) alloys, Acta Mater. 51 (2003) 6341–6357, https://doi.org/10.1016/j.actamat.2003.08.003.

[13] B.C. Hornbuckle, T.T. Sasaki, G.S. Bigelow, R.D. Noebe, M.L. Weaver, G.B. Thompson, Structure - property relationships in a precipitation strengthened Ni - 29.7Ti - 20Hf (at%) shape memory alloy, Mater. Sci. Eng. A 637 (2015) 63–69, https://doi.org/10.1016/j.msea.2015.03.123.

[14] B.C. Hornbuckle, R.D. Noebe, G.B. Thompson, Influence of Hf solute additions on the precipitation and hardenability in Ni-rich NiTi alloys, J. Alloy. Compd. 640 (2015) 449–454, https://doi.org/10.1016/j.jallcom.2015.04.002.

[15] M. Prasher, D. Sen, J. Bahadur, R. Tewari, M. Krishnan, Correlative SANS and TEM investigation on precipitation kinetics of H-phase in Ni50.3Ti29.7Hf20 high temperature shape memory alloy, J. Alloy. Compd. 779 (2019) 630–642, https://doi.org/10.1016/j.jallcom.2018.11.303.

[16] S.M. Saghaian, H.E. Karaca, H. Tobe, A.S. Turabi, S. Saedi, S.E. Saghaian, Y.I. Chumlyakov, R.D. Noebe, High strength NiTiHf shape memory alloys with

tailorable properties, Acta Mater. 134 (2017) 211–220, https://doi.org/10.1016/j.actamat.2017.05.065.

[17] X. Song, Y. Li, F. Zhang, S. Li, NiTiAl intermetallic alloys strengthened by Mo replacement, Chin. J. Aeronaut. 23 (2010) 715–719, https://doi.org/10.1016/S1000-9361(09)60274-0.

[18] F. Appel, M. Oehring, R. Wagner, Novel design concepts for gamma-base titanium aluminide alloys.pdf, Intermetallics 8 (2000) 1283–1312, https://doi.org/10.1016/S0966-9795(00)00036-4.

[19] Z. Wen, Y. Zhao, H. Hou, B. Wang, P. Han, The mechanical and thermodynamic properties of Heusler compounds Ni2XAl (X = Sc, Ti, V) under pressure and temperature: a first-principles study, Mater. Des. 114 (2017) 398–403, https://doi.org/10.1016/j.matdes.2016.11.005.

[20] P.W. Voorhees, G.B. McFadden, W.C. Johnson, On the morphological development of second-phase particles in elastically-stressed solids, Acta Metall. Et. Mater. 40 (1992) 2979–2992, https://doi.org/10.1016/0956-7151(92)90462-N.

[21] S.H. Hong, J.T. Kim, H.J. Park, Y.S. Kim, J.Y. Suh, Y.S. Na, K.R. Lim, C.H. Shim, J. M. Park, K.B. Kim, Influence of Zr content on phase formation, transition and mechanical behavior of Ni-Ti-Hf-Zr high temperature shape memory alloys, J. Alloy. Compd. 692 (2017) 77–85, https://doi.org/10.1016/j.jallcom.2016.09.023.

[22] J. Ma, I. Karaman, R.D. Noebe, High temperature shape memory alloys, Int. Mater. Rev. 55 (2010) 257–315.

[23] N. Singh, A. Talapatra, A. Junkaew, T. Duong, S. Gibbons, S. Li, H. Thawabi, E. Olivos, R. Arróyave, Effect of ternary additions to structural properties of NiTi alloys, Comput. Mater. Sci. 112 (2016) 347–355, https://doi.org/10.1016/j.commatsci.2015.10.029.

[24] D.H.D. Hsu, T.T. Sasaki, G.B. Thompson, M.V. Manuel, The effect of aluminum additions on the microstructure and thermomechanical behavior of NiTiZr shape-memory alloys, Met. Mater. Trans. A 43 (2012) 2921–2931, https://doi.org/10.1007/s11661-012-1167-8.

[25] D.R. Angst, P.E. Thoma, M.Y. Kao, The effect of hafnium content on the transformation temperatures of Ni49Ti51-xHfx. shape memory alloys, J. Phys. IV Fr. 05 (1995) C8–752, https://doi.org/10.1051/jp4/199558747.

[26] X.D. Han, R. Wang, Z. Zhang, D.Z. Yang, A new precipitate phase in a TiNiHf high temperature shape memory alloy, Acta Mater. 46 (1998) 273–281, https://doi.org/10.1016/S1359-6454(97)00187-0.

[27] D.R. Coughlin, P.J. Phillips, G.S. Bigelow, A. Garg, R.D. Noebe, M.J. Mills, Characterization of the microstructure and mechanical properties of a 50.3Ni-29.7Ti-20Hf shape memory alloy, Scr. Mater. 67 (2012) 112–115, https://doi.org/10.1016/j.scriptamat.2012.03.036.

[28] G.S. Bigelow, A. Garg, S.A.P. Ii, D.J. Gaydosh, R.D. Noebe, Load-biased shape-memory and superelastic properties alloy, Scr. Mater. 64 (2011) 725–728, https://doi.org/10.1016/j.scriptamat.2010.12.028.

[29] J. Jung, G. Ghosh, D. Isheim, G.B. Olson, Precipitation of heusler phase (Ni2TiAl) from B2-TiNi in Ni-Ti-Al and Ni-Ti-Al-X (X=Hf, Zr) alloys, Metall. Mater. Trans. A 34 (2003) 1221–1235, https://doi.org/10.1007/s11661-003-0233-7.

[30] R. Kainuma, I. Ohnuma, K. Ishida, Partition of alloying elements between γ (L12), η (DO24), β (B2) and H(L21) phases in the Ni-AI-Ti base systems, in: 1997. ⟨https://doi.org/10.1051/JCP/1997940978⟩.

[31] K. Oh-ishi, Z. Horita, M. Nemoto, Phase separation and lattice misfit in NiAl(β1)-Ni2AlTi(H)-NiTi(β2)system, Materials Transactions 38 (1997) 99–106. ⟨https://doi.org/10.2320/matertrans1989.38.99⟩.

[32] Y. Koizumi, Y. Ro, S. Nakazawa, H. Harada, NiTi-base intermetallic alloys strengthened by Al substitution, Mater. Sci. Eng. A 223 (1997) 36–41, https://doi.org/10.1016/S0921-5093(96)10508-6.

[33] T. Kurita, H. Matsumoto, K. Sakamoto, K. Tanji, H. Abe, Effect of aluminum addition on the transformation of NiTi alloy, J. Alloy. Compd. 396 (2005) 193–196, https://doi.org/10.1016/j.jallcom.2004.12.032.

[34] D.H.D. Hsu, B.C. Hornbuckle, B. Valderrama, F. Barrie, H.B. Henderson, G. B. Thompson, M.V. Manuel, The effect of aluminum additions on the thermal, microstructural, and mechanical behavior of NiTiHf shape memory alloys, J. Alloy. Compd. 638 (2015) 67–76, https://doi.org/10.1016/j.jallcom.2015.01.071.

[35] H. Chen, L.J. Zheng, F.X. Zhang, H. Zhang, Thermal stability and hardening behavior in superelastic Ni-rich Nitinol alloys with Al addition, Mater. Sci. Eng. A 708 (2017) 514–522, https://doi.org/10.1016/j.msea.2017.10.016.

[36] A. Evirgen, I. Karaman, J. Pons, R. Santamarta, R.D. Noebe, Role of nano-precipitation on the microstructure and shape memory characteristics of a new Ni50.3Ti34.7Zr15 shape memory alloy, Mater. Sci. Eng. A 655 (2016) 193–203, https://doi.org/10.1016/j.msea.2015.12.076.

[37] H.E. Karaca, S.M. Saghaian, G. Ded, H. Tobe, B. Basaran, H.J. Maier, R.D. Noebe, Y. I. Chumlyakov, Effects of nanoprecipitation on the shape memory and material properties of an Ni-rich NiTiHf high temperature shape memory alloy, Acta Mater. 61 (2013) 7422–7431, https://doi.org/10.1016/j.actamat.2013.08.048.

[38] H. Yu, Y. Qiu, M.L. Young, Influence of Ni4Ti3 precipitate on pseudoelasticity of austenitic NiTi shape memory alloys deformed at high strain rate, Mater. Sci. Eng. A 804 (2021) 140753, https://doi.org/10.1016/j.msea.2021.140753.

[39] A.V. Shuitcev, M.G. Khomutov, R.N. Vasin, L. Li, I.S. Golovin, Y.F. Zheng, Y. X. Tong, The role of H-phase in thermal hysteresis and shape memory properties in Ni50Ti30Hf20alloy, Scr. Mater. 230 (2023) 115391, https://doi.org/10.1016/j.scriptamat.2023.115391.

[40] ASTM E92-16., Standard Test Methods for Vickers Hardness and Knoop Hardness of Metallic Materials, ASTM Book of Standards 82 (2017) 1–27. ⟨https://doi.org/10.1520/E0092-16.Copyright⟩.

[41] L.A. Giannuzzi, F.A. Stevie, A review of focused ion beam milling techniques for TEM specimen preparation, Micron 30 (1999) 197–204, https://doi.org/10.1016/S0968-4328(99)00005-0.

[42] C.A. Schneider, W.S. Rasband, K.W. Eliceiri, NIH Image to ImageJ: 25 years of image analysis, Nat. Methods 9 (2012) 671–675, https://doi.org/10.1038/nmeth.2089.

[43] A. Baldan, Progress in Ostwald ripening theories and their applications to nickel-base superalloys. Part I: Ostwald ripening theories, J. Mater. Sci. 37 (2002) 2171–2202, https://doi.org/10.1023/A:1015388912729.

[44] J. Svoboda, F.D. Fischer, Generalization of the Lifshitz-Slyozov-Wagner coarsening theory to non-dilute multi-component systems, Acta Mater. 79 (2014) 304–314, https://doi.org/10.1016/j.actamat.2014.05.042.

[45] C. Ai, X. Zhao, J. Zhou, H. Zhang, L. Liu, Y. Pei, S. Li, S. Gong, Application of a modified Ostwald ripening theory in coarsening of γ' phases in Ni based single crystal superalloys, J. Alloy. Compd. 632 (2015) 558–562, https://doi.org/10.1016/j.jallcom.2015.01.215.

[46] T. Gladman, Precipitation hardening in metals, Mater. Sci. Technol. 15 (1999) 30–36, https://doi.org/10.1179/026708399773002782.

[47] D. Seidman, E. Marquis, D. Dunand, Precipitation strengthening at ambient and elevated temperatures of heat-treatable Al (Sc) alloys, Acta Mater. 50 (2002) 4021–4035, https://doi.org/10.1016/S1359-6454(02)00201-X.

[48] T. Ezaz, J. Wang, H. Sehitoglu, H.J. Maier, Plastic deformation of NiTi shape memory alloys, Acta Mater. 61 (2013) 67–78, https://doi.org/10.1016/j.actamat.2012.09.023.

[49] J. Pfetzing-Micklich, R. Ghisleni, T. Simon, C. Somsen, J. Michler, G. Eggeler, Orientation dependence of stress-induced phase transformation and dislocation plasticity in NiTi shape memory alloys on the micro scale, Mater. Sci. Eng.: A 538 (2012) 265–271, https://doi.org/10.1016/j.msea.2012.01.042.

[50] G. Mazzolai, Recent progresses in the understanding of the elastic and anelastic properties of H-free, H-doped and H-contaminated NiTi based alloys, AIP Adv. 1 (2011) 040701, https://doi.org/10.1063/1.3655567.

[51] K. Torronen, A method for measuring the planar interparticle distance between plate-like precipitates many microstructural features such as dislocations, second-phase par-, Metallography 13 (1980) 329–344.

[52] W.J. Buehler, J.V. Gilfrich, R.C. Wiley, Effect of low-temperature phase changes on the mechanical properties of alloys near composition TiNi, J. Appl. Phys. 34 (1963) 1475–1477, https://doi.org/10.1063/1.1729603.

[53] K. Otsuka, X. Ren, Recent developments in the research of shape memory alloys, Intermetallics 7 (1999) 511–528.

[54] T. Umale, D. Salas, B. Tomes, R. Arroyave, I. Karaman, The effects of wide range of compositional changes on the martensitic transformation characteristics of NiTiHf shape memory alloys, Scr. Mater. 161 (2019) 78–83, https://doi.org/10.1016/j.scriptamat.2018.10.008.

[55] R. Santamarta, R. Arróyave, J. Pons, A. Evirgen, I. Karaman, H.E. Karaca, R. D. Noebe, TEM study of structural and microstructural characteristics of a precipitate phase in Ni-rich Ni-Ti-Hf and Ni-Ti-Zr shape memory alloys, Acta Mater. 61 (2013) 6191–6206, https://doi.org/10.1016/j.actamat.2013.06.057.

[56] A. Evirgen, J. Pons, I. Karaman, R. Santamarta, R.D. Noebe, H-Phase precipitation and martensitic transformation in Ni-rich Ni–Ti–Hf and Ni–Ti-Zr high-temperature shape memory alloys, Shap. Mem. Superelast. 4 (2018) 85–92, https://doi.org/10.1007/s40830-018-0165-0.

[57] S. Kumar Makineni, S. Sugathan, S. Meher, R. Banerjee, S. Bhattacharya, S. Kumar, K. Chattopadhyay, Enhancing elevated temperature strength of copper containing aluminium alloys by forming L12 Al3Zr precipitates and nucleating θ'' precipitates on them, Sci. Rep. 7 (2017) 11154, https://doi.org/10.1038/s41598-017-11540-2.

[58] Q. Gao, Y. Zhang, H. Zhang, H. Li, F. Qu, J. Han, C. Lu, B. Wu, Y. Lu, Y. Ma, Precipitates and particles coarsening of 9Cr–1.7W–0.4Mo–Co ferritic heat-resistant steel after isothermal aging, Sci. Rep. 7 (2017) 5859, https://doi.org/10.1038/s41598-017-06191-2.

[59] S. Fashu, B. Huang, N. Wang, Modification of precipitate coarsening kinetics by intragranular nanoparticles—a phase field study, Metals 12 (2022) 892, https://doi.org/10.3390/met12060892.

[60] A. Devaux, L. Nazé, R. Molins, A. Pineau, A. Organista, J.Y. Guédou, J.F. Uginet, P. Héritier, Gamma double prime precipitation kinetic in Alloy 718, Mater. Sci. Eng. A 486 (2008) 117–122, https://doi.org/10.1016/j.msea.2007.08.046.

[61] X. Li, N. Saunders, A.P. Miodownik, The coarsening kinetics of γ prime particles in nickel-based alloys, Metall. Mater. Trans. A Phys. Metall. Mater. Sci. 33 (2002) 3367–3374, https://doi.org/10.1007/s11661-002-0325-9.

[62] P. Zhang, S.X. Li, Z.F. Zhang, General relationship between strength and hardness, Mater. Sci. Eng.: A 529 (2011) 62–73, https://doi.org/10.1016/j.msea.2011.08.061.

[63] T. Gladman, Precipitation hardening in metals, Mater. Sci. Technol. 15 (1999) 30–36, https://doi.org/10.1179/026708399773002782.

[64] M.D. Bender, G.B. Olson, Designing a Precipitation-Strengthened, Superelastic, TiNi-Based Alloy for Endovascular Stents, in: G.B. Olson, D.S. Lieberman, A. Saxena (Eds.), ICOMAT, John Wiley & Sons, Inc., Hoboken, NJ, USA, 2013, pp. 159–166, https://doi.org/10.1002/9781118803592.ch22.

[65] B.C. Hornbuckle, X.X. Yu, R.D. Noebe, R. Martens, M.L. Weaver, G.B. Thompson, Hardening behavior and phase decomposition in very Ni-rich Nitinol alloys, Mater. Sci. Eng. A 639 (2015) 336–344, https://doi.org/10.1016/j.msea.2015.04.079.